Biosensors and Bioelectronics 160 (2020) 112210

Contents lists available at ScienceDirect

Biosensors and Bioelectronics

journal homepage: http://www.elsevier.com/locate/bios

An antibody-aptamer sandwich cathodic photoelectrochemical biosensor for the detection of progesterone

Yuhan Zhu [a], Zuwei Xu [b], Jie Gao [a], Weihao Ji [a], Jingdong Zhang [a,*]

[a] Key Laboratory of Material Chemistry for Energy Conversion and Storage (Ministry of Education), School of Chemistry and Chemical Engineering, Huazhong University of Science and Technology, Luoyu Road 1037, Wuhan, 430074, PR China

[b] State Key Laboratory of Coal Combustion, School of Energy and Power Engineering, Huazhong University of Science and Technology, Luoyu Road 1037, Wuhan, 430074, PR China

ARTICLE INFO

Keywords:
Carbon dots-graphene oxide composites
Au–CuO–Cu_2O
Antibody-aptamer sandwich assay
Cathodic photoelectrochemical biosensor
Progesterone

ABSTRACT

The progesterone (P4) level in body fluids can act as an indicator for early pregnancy diagnosis and offers insight into mammalian somatic function. In this work, we designed an antibody-aptamer based sandwich assay as a cathodic photoelectrochemical (PEC) biosensor for P4 detection. The composites of carbon dots and graphene oxide (CDs-GO) with favorable cathodic photocurrent response were used as photoactive materials on which the antibody (Ab) of P4 was immobilized. Meanwhile, high affinity truncated P4 aptamer was immobilized on Au–CuO–Cu_2O to act as a bioconjugate. When P4 was present, the aptamer-Au-CuO-Cu_2O bioconjugate could amplify the cathodic photocurrent of CDs-GO modified electrode through Ab-P4-aptamer interactions. Under optimum conditions, the cathodic photocurrent of the constructed PEC biosensor was found to increase linearly with P4 in a wide concentration range from 0.5 nM to 180 nM, with a low detection limit (3S/N) of 0.17 nM. The proposed cathodic PEC sensing platform demonstrated high selectivity, satisfying reproducibility, good stability. The sensor was successfully applied in the determination of P4 in human serum samples.

1. Introduction

Due to their tunable photoluminescence, high photostability, good biocompatibility, low toxicity and easy functionalization, carbon dots (CDs) have been widely employed in bioimaging, biosensing, nanomedicine, electrocatalysis, photocatalysis, photoelectrocatalysis, light-emitting diode, solar cell, battery and supercapacitor (Hu et al., 2019; Yuan et al., 2016; Zhang and Yu, 2016). Recently, CDs have served as an excellent supplement to traditional metal oxide semiconductor nanomaterials in construction of photoelectrochemical (PEC) sensors. Although CDs are generally considered as photoanodic material, small cathodic photocurrents have been observed at negative potentials applied on CDs-modified ITO electrode (Liu et al., 2015) and CDs@mesoporous silica-coated Au electrode (Li et al., 2018). Such a photocathodic property of CDs should be very useful to the development of cathodic PEC biosensor which can avoid the intrinsic oxidation reactions of absorbed reductive species at the photoanode/electrolyte interface in anodic PEC sensor (Fan et al., 2016; Teng et al., 2018).

As a steroid hormone secreted by the ovary, progesterone (P4) plays a critical role in the maintenance and regulation of the female menstrual cycle, embryogenesis, pregnancy and mammogenesis for the preparation of lactation (Graham and Clarke, 1997; Lishko et al., 2011). P4 has been not only considered as an important factor influencing the reproduction performance of dairy cows in veterinary medicine (Claus et al., 1983), but also extensively applied in pharmaceutical and clinical therapies for humans (Dai et al., 2002; Erny et al., 1986; Hargrove et al., 1989). However, the abuse of P4 may cause undesirable side effects like asthenia, emotional depression, breast discomfort and potential carcinogenicity (Greendale et al., 1998; Herzog, 1995; Kim et al., 2013). Additionally, the living body can partially retain P4 even though high dose of this hormone is consumed, while the excess P4 is subsequently released to the environment. Actually, P4 is excreted at high concentration among hormones and has been detected in the aqueous environment (Ojoghoro et al., 2017). It has been considered as a representative of endocrine disrupting compounds (EDCs) that may do harm for wildlife survival and human health. Therefore, sensitive analytical methods for P4 monitoring are highly demanded in clinical medicine, animal husbandry and environmental protection. Different instrumental techniques including chromatography (Tölgyesi et al., 2010; Zhang and Fent, 2018), fluorescence (Trapiella-Alfonso et al.,

* Corresponding author.
E-mail address: zhangjd@mail.hust.edu.cn (J. Zhang).

https://doi.org/10.1016/j.bios.2020.112210
Received 6 February 2020; Received in revised form 5 April 2020; Accepted 9 April 2020
Available online 15 April 2020

2011), colorimetry (Du et al., 2016) and electrochemistry (Das and Sangaranarayanan, 2018; Gevaerd et al., 2018; Serafín et al., 2019) have been developed for P4 detection.

Although sandwich assays with antibody-antigen-antibody (Ab-Ag-Ab) construction have been widely used for signal amplification in sensing applications (Doldán et al., 2016; Fan et al., 2017), they are unfavorable to PEC detection because the immunocomplex with dual Ab showing poor conductivity would cause unsatisfactory steric hindrance effect on the transfer of photogenerated carriers and diffusion of reactive species at electrode surface. Moreover, the dual Ab strategy is more suitable for the detection of macromolecular targets rather than low molecular compounds, because the steric hindrance leads to the difficulty of simultaneous binding of a small molecule to two Abs (Zuo et al., 2009). Actually, as an alternative to Ab, aptamer has flexibility in structure design and high specific affinity to various targets including small molecules, peptides, proteins and cells (Iliuk et al., 2011; Willner and Zayats, 2007). By using aptamer instead of Ab, sandwich assays of Ab-aptamer or aptamer-aptamer have become desirable configurations (Song et al., 2008; Wu et al., 2014b; Zhao et al., 2015). Generally, in order to effectively improve the sensing performance, the secondary aptamer served as a reporter probe in such sandwich assays has been integrated with enzyme, mimic enzyme, metal nanoparticles or semiconductor materials (Golub et al., 2015; Sharma et al., 2012; Wu et al., 2014a). The aptamer conjugated with n-type semiconductors such as CdS and Ag_2S have been employed to develop sandwich signal-amplified PEC sensing strategies (Golub et al., 2009; Qiu et al., 2018).

Herein, we proposed an Ab-aptamer sandwich PEC biosensor for sensitive detection of P4 using CDs as photocathodic material for the first time. In such a design, the Ab of P4 was immobilized on the electrode modified with CDs and graphene oxide (GO) composites through a carbodiimide-assisted amidation reaction with abundant carboxyl groups on the edge and surface of GO sheets (Song et al., 2018; Zhang et al., 2013). On the other hand, a bioconjugate was prepared by assembling high-affinity P4-binding aptamer on Au nanoparticles-decorated CuO–Cu_2O heterojunction. When target P4 was present, the aptamer-Au-CuO-Cu_2O bioconjugate could be immobilized on the Ab/CDs-GO modified electrode via the Ab-P4-aptamer interactions. Since Au–CuO–Cu_2O composites possessed high photocathodic activity, they could amplify the cathodic photocurrent of CDs-GO after the formation of sandwich structure. Thus, a cathodic "signal-on" PEC sensing platform was successfully constructed for highly sensitive and selective detection of P4.

2. Experimental section

2.1. Chemicals

P4, estrone (E1), β-estradiol (E2), estriol (E3), epinephrine (EP), 17α-ethynylestradiol (EE2), diethylstilbestrol (DES), *N*-(3-Dimethyl aminopropyl)-*N*′-ethylcarbodiimide hydrochloride (EDC) and *N*-hydroxysuccinimide (NHS) were acquired from Aladdin Bio-Chem Technology Co., Ltd. (Shanghai, China). Citric acid, ethylenediamine, copper nitrate trihydrate ($Cu(NO_3)_2{\cdot}3H_2O$) and other reagents of analytical grade were supplied by Sinopharm Chemical Reagent Co. Ltd. (Shanghai, China). Bovine serum albumin (BSA) was obtained from Shanghai Regal Biology Technology Co, Ltd. (Shanghai, China). Polyclonal Ab of P4 was provided by Cloud-Clone Corp. (Wuhan, China). P4-binding DNA aptamer with sequence of 5′-GATTA ACATT AGCCC ACCGC CCACC-C6-SH-3′ (Alhadrami et al., 2017) was synthesized by Shanghai Sangon Biotech Co., Ltd. (Shanghai, China). The stock solutions of Ab and aptamer were diluted with 10 mM phosphate buffer solution (PBS, pH 7.4) and stored at 4 °C for further use. The EDC/NHS solution containing 0.01 M EDC and 0.002 M NHS was prepared with 10 mM PBS (pH 7.4). Doubly distilled water (resistivity of 18.2 MΩ cm) was used throughout the experiment.

2.2. Synthesis of CDs-GO nanocomposites

The CDs were synthesized by a hydrothermal process. Briefly, 0.53 g citric acid was dissolved in 10 mL deionized water, and then 168 μL of ethylenediamine was added dropwise under gentle magnetic stirring. The homogeneous solution was transferred into a 20-mL Teflon-lined autoclave, and then sealed in a stainless steel tank and further heated to 180 °C in an electric oven for 5 h. After the reactor was naturally cooled to room temperature, the red-brown product was collected by centrifugation, washed several times with anhydrous ethanol, and dried at 60 °C.

GO was synthesized by modified Hummers method from graphite powder as described previously (Wei et al., 2011). GO was dispersed in distilled water under ultrasonic agitation for 2 h to give a 2 mg mL^{-1} GO suspension. The CDs-GO composites were prepared by directly injecting a certain volume of GO suspension (2 mg mL^{-1}) to CDs aqueous solution (2 mg mL^{-1}) under vigorous stirring. The as-prepared nanocomposites with different weight contents of GO were labeled as CDs-x%GO, where x referred to the weight percentage of GO to CDs.

2.3. Preparation of aptamer-Au-CuO-Cu_2O bioconjugate

The CuO–Cu_2O heterojunction was synthesized by one-step flame spray pyrolysis (FSP) as described previously (Zhu et al., 2017). Au nanoparticles were prepared by a sodium citrate reduction method according to a previous report (Grabar et al., 1995) with a little modification. Briefly, 20 mL of 1 mM $HAuCl_4$ solution was brought to boil in a 50-mL round-bottom flask equipped with condenser pipe. Under vigorous stirring, 2 mL of 38.8 mM sodium citrate was rapidly added into the vortex of the solution, and the color of mixed solution changed from pale yellow to zinzolin in 1 min. After boiling reflux for another 20 min, the wine-red solution of Au nanoparticles was cooled down to room temperature with stirring. After 1 mg CuO–Cu_2O powder was dispersed evenly in 1 mL of Au nanoparticles solution with the aid of ultrasonication, the mixture was continuously stirred for 1 h. The suspension was centrifuged and washed with distilled water. The product was re-dispersed in 1 mL PBS (10 mM, pH 7.4), and then 10 μL of 10 μM 3′-sulfhydryl-modified aptamer of P4 was added under vigorous stirring to allow the loading of aptamer on Au–CuO–Cu_2O via gold-sulfur bonding interaction. After incubation for 30 min, the product was centrifuged and washed with 10 mM PBS (pH 7.4). The stock solution of aptamer-Au-CuO-Cu_2O bioconjugate was prepared with 10 mM PBS (pH 7.4) and stored at 4 °C for further use.

2.4. Fabrication of biosensor

Scheme 1 illustrates the fabrication of the photocathodic biosensor. Before modification, bare glass carbon electrode (GCE) was polished with 0.05 μm alumina slurry on a chamois, followed by ultrasonic cleaning with ethanol and doubly distilled water successively, and then dried with nitrogen gas. The mirror-like smooth GCE surface with an exposed geometric surface area of 0.096 cm^2 was coated with 10 μL of CDs-GO suspension and dried at 60 °C to form a homogeneous film. Subsequently, the electrode surface was treated with EDC/NHS solution to activate carboxyl group for 0.5 h at 37 °C. The excessive EDC/NHS was removed by rinsing with PBS (pH 7.4). Then, 5 μL of 8 μg mL^{-1} Ab was dropped on the electrode surface and incubated for 4 h at 37 °C to form Ab/CDs-GO modified electrode. After loosely bounded Ab was washed off, the modified electrode was treated with 4 μL of 1 wt% BSA in 10 mM PBS (pH 7.4) for 1 h at 37 °C to block nonspecific binding sites and then washed with PBS carefully. BSA was chosen as the blocking reagent, because of its simple composition, low cost and easy acquisition in the fabrication of PEC immunosensors (Zhao et al., 2018). Next, P4 sample solution was dropped on Ab/CDs-GO modified electrode and incubated for 1 h at 37 °C, followed by washing away physically adsorbed P4. Finally, the electrode was incubated with 5 μL of

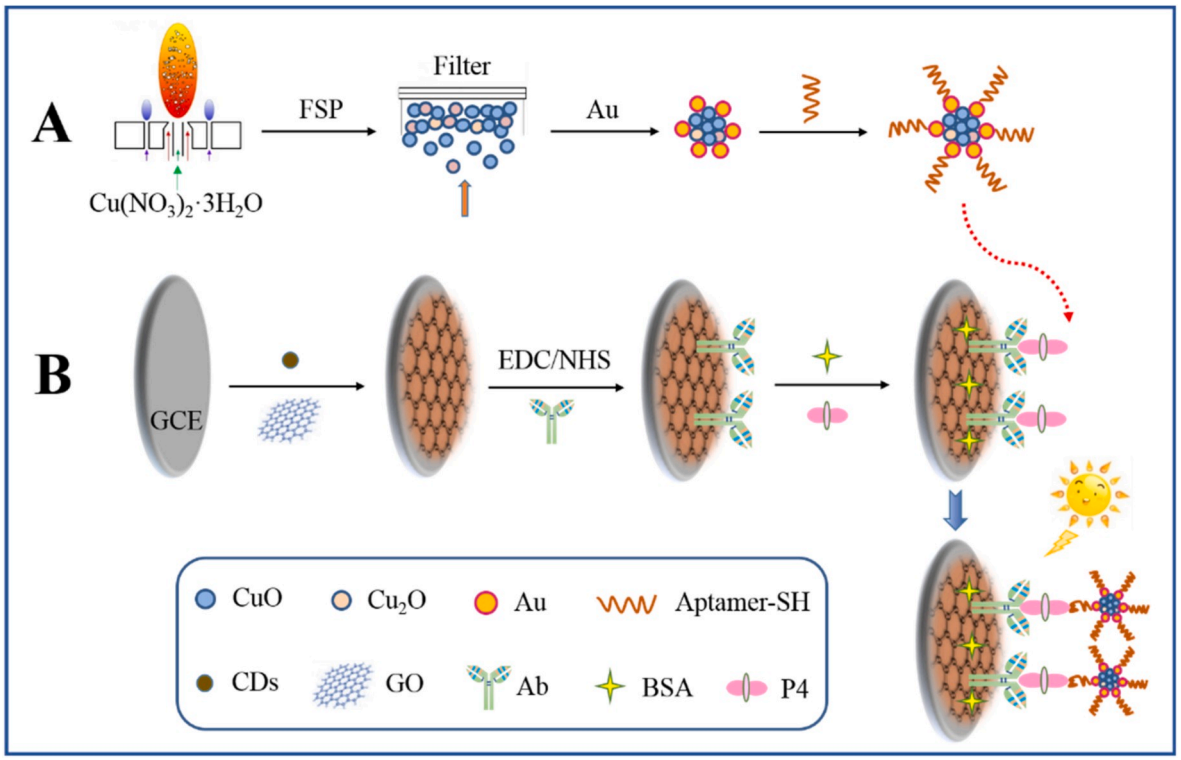

Scheme 1. Schematic illustration for (A) the preparation process of aptamer-Au-CuO-Cu_2O bioconjugate as signal amplification element and (B) the fabrication of cathodic PEC sensor for P4 detection using Ab-aptamer-based sandwich assay.

aptamer-Au-CuO-Cu_2O bioconjugate for 40 min at 37 °C to achieve an Ab-aptamer sandwich assay. After rinsing with 10 mM PBS (pH 7.4) and drying naturally, the obtained aptamer-Au-CuO-Cu_2O/P4/Ab/CDs-GO modified electrode was stored at 4 °C in dry state for further measurement.

2.5. Apparatus and procedure

The surface morphology characterization was performed on a Gemini 300 field emission scanning electron microscope (SEM) (Carl Zeiss, Germany) equipped with X-Max 50 energy dispersive spectroscopy (EDS) (Oxford, UK). Transmission electron microscopic (TEM), high-resolution transmission electron microscopic (HRTEM) and high-angle annular dark-field scanning transmission electron microscopic (HAADF-STEM) images as well as relevant EDS spectra were obtained on a Talos F200X instrument (FEI, Netherlands). X-ray diffraction (XRD) analysis was carried out on a Bruker D8 Advance X-ray diffractometer (Bruker Instruments, Germany) with Cu K_α radiation. The Fourier transform infrared (FT-IR) spectra were recorded with an INVENIO-R FT-IR spectrometer (Bruker Instruments, Germany). X-ray photoelectron spectroscopy (XPS) analysis was performed on an AXIS ULTRA DLD-600W spectrometer (Kratos Company, England). The UV–visible (UV–Vis) absorption spectra were measured on a TU-1900 spectrometer (Beijing Purkinje General Instrument Company, China).

The PEC measurements were carried out on a CHI830C electrochemical working station (Shanghai Chenhua Instrument Co. Ltd., China) using a conventional three-electrode system. In PEC system, a CEL-S500/350 xenon lamp (CEAULIGHT Co., China) with an optical filter ($\lambda > 420$ nm) was employed as the irradiation source, and the distance between the lamp and working electrode surface was 10 cm.

3. Results and discussion

3.1. Characterization of CDs-GO

Fig. 1 shows the SEM images of various materials modified electrodes. It is seen that GO displays a typical sheet structure with wrinkles (Fig. 1A). For CDs modified electrode, the surface morphology appears a haphazardly branched shape (Fig. 1B), due to the aggregation of CDs. When the electrode is modified with CDs-GO composites, a relatively uniform membrane is observed (Fig. 1C), implying that GO reduces the aggregation of CDs in the composites. Meanwhile, the as-prepared materials were also studied by TEM. As can be seen in Fig. 1D, the GO is stacked randomly and exhibits two-dimensional sheets with chiffon-like ripples and wrinkles. The CDs display as monodispersed qusi-spherical particles (Fig. 1E) with an average diameter of 2.58 ± 0.37 nm (Fig. S1), and the lattice spacing of 0.21 nm revealed by the HRTEM image of CDs is assigned to the (100) plane of graphitic carbon (Fig. S2). In the CDs-GO composites, CDs are evenly distributed on the lamellar structure of GO (Fig. 1F).

The crystalline phases of the prepared materials were analyzed by XRD. As illustrated in curve a in Fig. 1G, GO exhibits a sharp diffraction peak at 10.64° assigning to its characteristic (001) crystal plane, showing an increased interlayer spacing compared with graphite due to the introduction of many oxygen-containing groups between layers. The XRD pattern of CDs shows a broad diffraction peak around 26.2° (curve b in Fig. 1G), which can be indexed to the (002) plane of graphitic structure (Fan et al., 2018). In the XRD pattern of CDs-GO composites (curve c in Fig. 1G), the original diffraction peaks of individual material are widened and slightly moved to lower angles, indicating enlarged interlayer spacings derived from the interposition of CDs into wrinkle layers of GO.

The surface chemical features and functional groups of the as-obtained CDs-GO composites were investigated by FT-IR. The spectral line of GO (curve a in Fig. 1H) exhibits the characteristic absorption peaks centered around 3420 cm^{-1} and 1406 cm^{-1} assigned to the

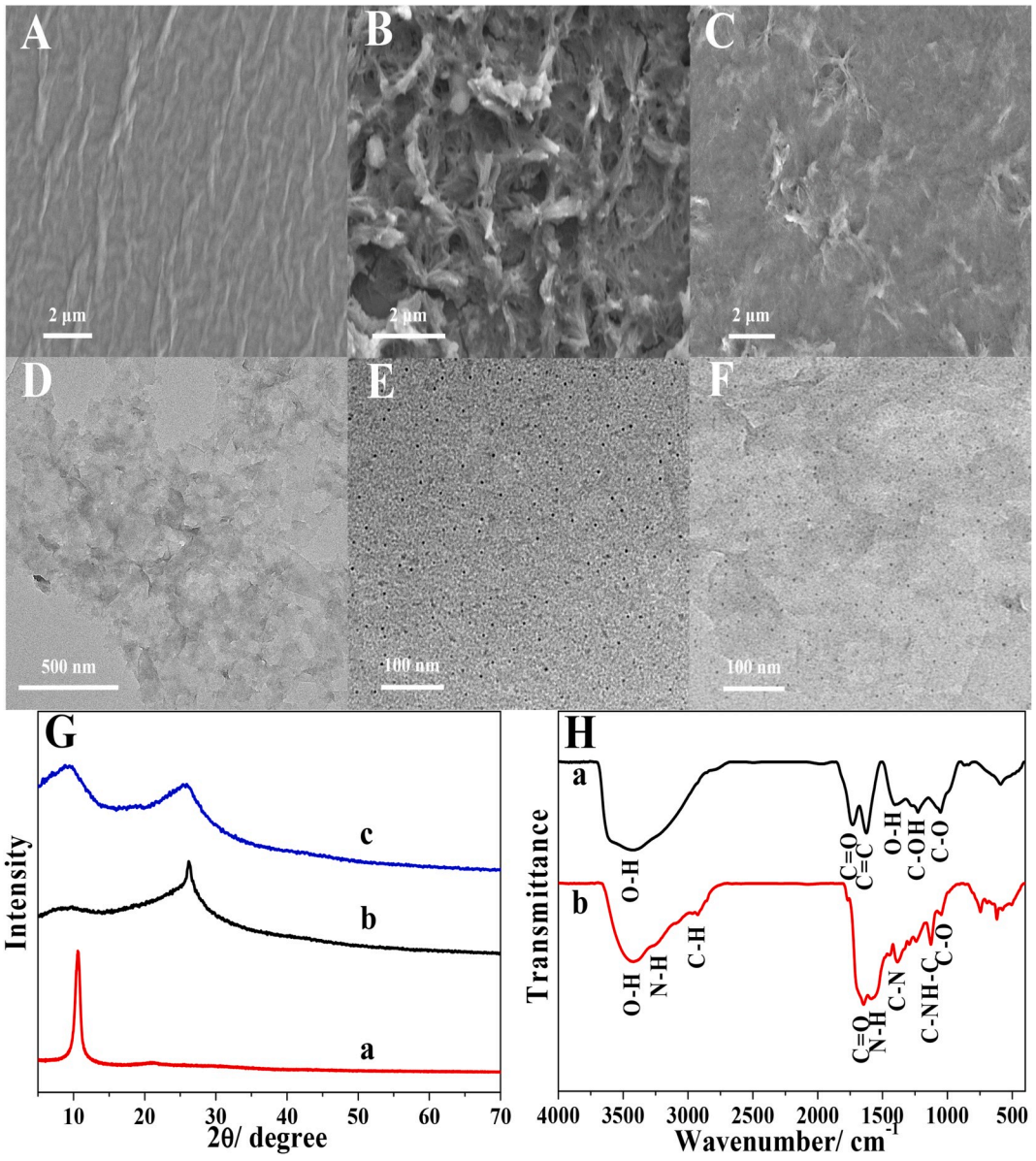

Fig. 1. SEM (A–C) and TEM (D–F) images of (A, D) GO, (B, E) CDs and (C, F) CDs-GO. (G) XRD patterns of (a) GO, (b) CDs and (c) CDs-GO composites. (H) FT-IR spectra of (a) GO and (b) CDs-GO.

stretching vibration and bending vibration of O–H. The other peaks appear at 1730 cm^{-1}, 1627 cm^{-1}, 1228 cm^{-1} and 1054 cm^{-1}, corresponding to the stretching vibrations of C═O, C═C, C–OH and C–O, respectively (Hontoria-Lucas et al., 1995; Li et al., 2012). The FTIR spectrum of CDs-GO, by contrast, displays the representative absorption peaks of nitrogen doped carbon dots besides the partially retained absorption peaks of GO. As illustrated in curve b of Fig. 1H, new absorption bands at 3257 cm^{-1} and 2923 cm^{-1} are attributed to the contribution of stretching vibrations of N–H and C–H bonds. The characteristic band around 1646 cm^{-1} is assigned to C═O stretching vibration in primary and/or tertiary amides (Travlou et al., 2018). Meanwhile, the absorption peaks at 1588 cm^{-1}, 1385 cm^{-1} and 1130 cm^{-1} are ascribed to the bending vibration of N–H, C–N and stretching vibrations of C–NH–C, which further confirm the abundant amide functional groups in N-doped CDs (Liu et al., 2017; Zhu et al., 2013). These hydrophilic groups can bring about excellent water solubility for GO and the N-CDs without further modification. Thus, the FT-IR analysis suggests that the coupling of GO with CDs in the composites is successfully achieved.

3.2. *Characterization of Au–CuO–Cu_2O*

The morphology of Au–CuO–Cu_2O composites was observed by SEM. As illustrated in Fig. 2A, the CuO–Cu_2O heterojunction exhibits abundant and relatively homogeneous nanoparticles which forms a porous film on the substrate surface. In Au–CuO–Cu_2O, some Au nanoparticles are introduced and combined closely with Cu_xO nanoparticles (Fig. 2B). The TEM analysis indicates that the sizes of Cu_xO particles are less than 10 nm and Au nanoparticles are about 13 nm, respectively (Fig. 2C). In HRTEM image (Fig. 2D), the lattice spacings of 0.232 nm and 0.246 nm correspond to the (111) planes of CuO and Cu_2O, respectively; and the lattice spacings of 0.235 nm and 0.204 nm are assigned to the (111) and (200) planes of Au. Further, the morphology and structure feature of Au–CuO–Cu_2O were analyzed by HAADF-STEM. As shown in Fig. 2E, the Au nanoparticles brighter than close-connected Cu_xO particles are clearly observed, owing to heavier atomic weight of Au than Cu (Mazumder et al., 2010). The compositional architecture of these nanoparticles is further confirmed by the HAADF-EDS mapping (Fig. 2E) and spectrum (Fig. 2F), suggesting that the Au–CuO–Cu_2O composites

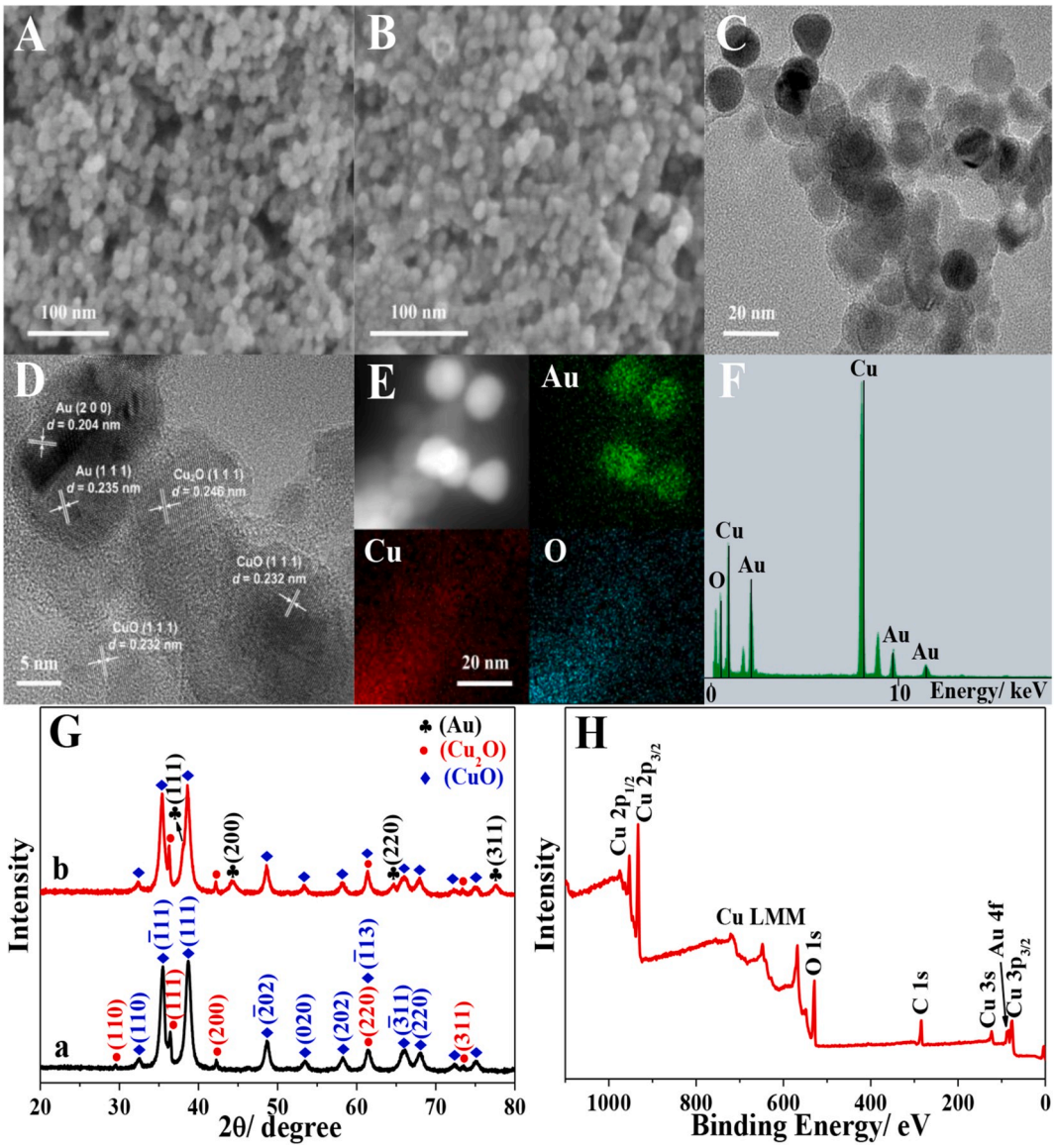

Fig. 2. SEM images of (A) CuO–Cu_2O and (B) Au–CuO–Cu_2O. (C) TEM, (D) HRTEM, (E) HAADF-STEM images and elemental mapping of Au–CuO–Cu_2O. (F) Corresponding EDS spectrum of selected HAADF-STEM regions. (G) XRD patterns of (a) CuO–Cu_2O and (b) Au–CuO–Cu_2O. (H) XPS survey spectrum of Au–CuO–Cu_2O.

are successfully synthesized.

On the other hand, the XRD patterns of CuO–Cu_2O and Au–CuO–Cu_2O composites were investigated. As shown in curve a in Fig. 2G, the pure CuO–Cu_2O exhibits the typical diffraction patterns responding to the monoclinic phase of CuO (JCPDS card no. 05–0661) and cubic phase structure of Cu_2O (JCPDS card no. 05–0667) (Zhu et al., 2017). For Au–CuO–Cu_2O sample (curve b in Fig. 2G), some new diffraction peaking at 38.2°, 44.3°, 64.6° and 77.6° can be indexed to the (111), (200), (220) and (311) crystal planes in cubic phase of Au (JCPDS card no. 01–1172). No other additional diffraction peaks are identified, manifesting that no other impurities are introduced in the composite material.

The chemical composition of Au–CuO–Cu_2O composites was analyzed by XPS. The survey XPS spectrum (Fig. 2H) clearly manifests that only Cu, O, Au and environmental C elements are detected in the sample without other impurities. The high-resolution XPS spectrum of Cu 2p (Fig. S3) shows that the peaks at 933.0 eV and 952.77 eV are ascribed to the Cu $2p_{3/2}$ and Cu $2p_{1/2}$ of Cu_2O. Despite the shake-up satellite peaks located at 941.0 eV, 943.8 eV and 962.7 eV, the two peaks with binding energies of 934.75 eV and 954.5 eV can also reveal the existence of CuO (Li et al., 2017). The O 1s spectrum (Fig. S4) could be fitted into two peaks. The dominant peak at 531.9 eV is ascribed to the Cu–O bond of CuO and/or Cu_2O, and the another peak at 535.86 eV is related to surface hydroxyl group. As for Au 4f spectrum (Fig. S5), two peaks centered at 84.3 eV and 87.98 eV correspond to $4f_{7/2}$ and Au $4f_{5/2}$ of metallic gold in the zero valent state, respectively (Murdoch et al., 2011). The results are in accordance with those of HRTEM, HAADF and XRD, further demonstrating the successful preparation of the Au–CuO–Cu_2O nanocomposites.

3.3. Optical and photocurrent analysis

The UV–Vis absorption spectra were recorded to investigate the optical adsorption properties of the photoactive materials. As illustrated in curve a in Fig. 3A, pure GO shows weak absorption. In the absorption spectrum of CDs (curve b in Fig. 3A), two absorption bands centered around 335 nm and 442 nm are observed, which can be attributed to the n-π* transition of the C═O bond and surface/molecule center,

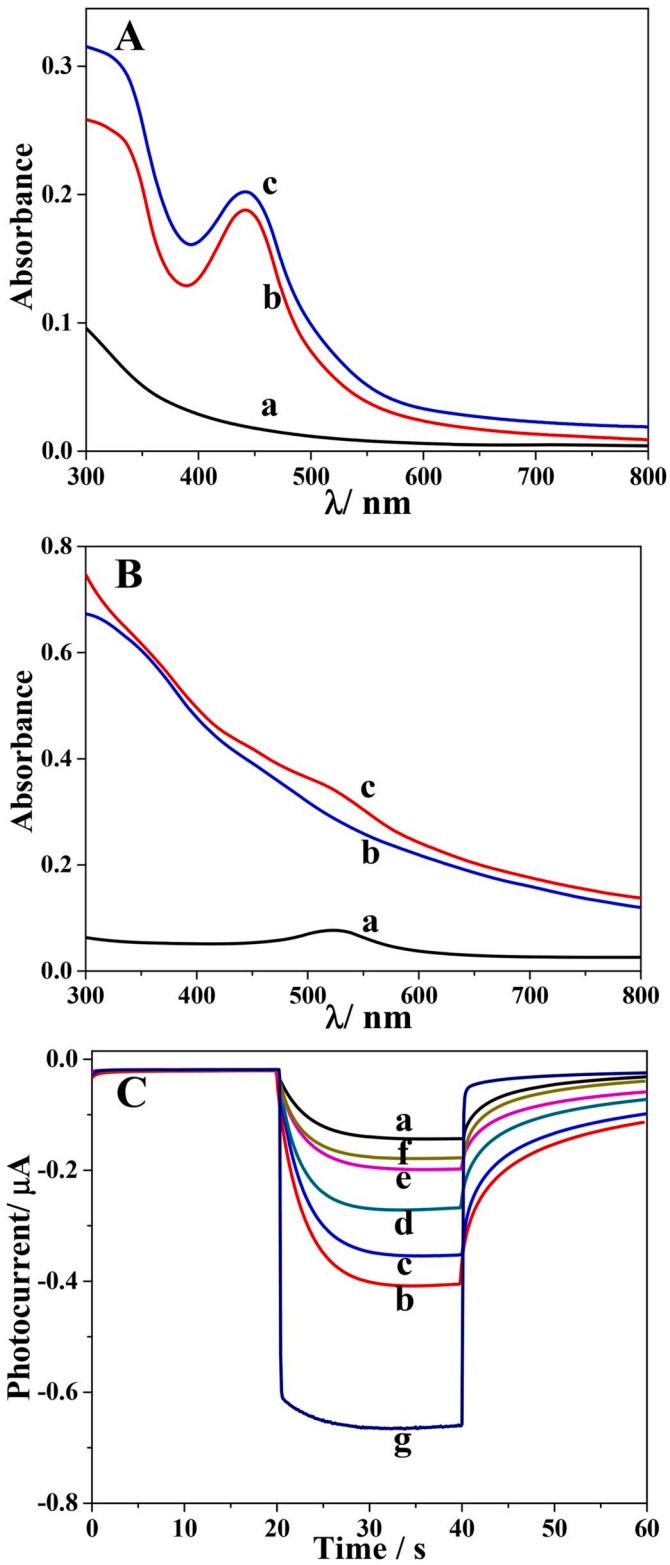

Fig. 3. (A) UV–Vis absorption spectra of (a) GO, (b) CDs and (c) CDs-GO. (B) UV–Vis absorption spectra of (a) Au, (b) CuO–Cu_2O and (c) Au–CuO–Cu_2O. (C) Photocurrent responses of different modified electrodes recorded in 0.1 M PBS (pH 7.4) at a bias potential of 0 V: (a) CDs/GCE, (b) CDs-GO/GCE, (c) EDC-NHS/CDs-GO/GCE, (d) Ab/EDC-NHS/CDs-GO/GCE, (e) BSA/Ab/EDC-NHS/CDs-GO/GCE, (f) P4/BSA/Ab/EDC-NHS/CDs-GO/GCE and (g) aptamer-Au-CuO-Cu_2O/P4/BSA/Ab/EDC-NHS/CDs-GO/GCE. The P4 concentration used in (f) and (g) was 50 nM.

respectively (Xu et al., 2014; Zhang et al., 2012). Moreover, the absorption of CDs is obviously stronger than that of GO. When CDs and GO form composites, the absorption is further enhanced in the visible region (curve c in Fig. 3A), endowing the photoactive nanomaterials with an advantage in the construction of photoelectrode. On the other hand, the UV–Vis absorption spectra of Au–CuO–Cu_2O composites were also recorded. The Au colloidal solution shows a characteristic absorption peak at 524 nm (curve a in Fig. 3B), assigned to a plasmon band of spherical Au nanoparticles (Jain et al., 2007; Jana et al., 2001). The absorption of CuO–Cu_2O heterojunction (curve b in Fig. 3B) above 400 nm is obviously enhanced after formation of Au–CuO–Cu_2O composites (curve c in Fig. 3B), due to the surface plasmon resonance of Au nanoparticles. Therefore, the Au–CuO–Cu_2O nanocomposites should be favorable to the amplification of PEC signal under visible light illumination.

In order to evaluate the PEC performance of the as-prepared materials, the photocurrent responses of various modified electrodes were recorded at a bias potential of 0 V under visible light irradiation. As can be seen, the CDs modified electrode generates considerable cathodic photocurrent (curve a in Fig. 3C), due to the reduction of dissolved oxygen by photogenerated electrons on CDs. The photocurrent of CDs-GO modified electrode (curve b in Fig. 3C) is almost two times higher than that of CDs/GCE, owing to the improved light absorption of CDs by GO in the composites. However, the photocurrent of CDs-GO/GCE decreases continuously after activating carboxyl groups with EDC/NHS (curve c in Fig. 3C), incubating with P4-binding Ab (curve d in Fig. 3C), blocking with BSA (curve e in Fig. 3C) and incorporating P4 as "sandwich center" (curve f in Fig. 3C). This can be attributed to the increased steric hindrance effect that inhibits the mass transfer of oxygen to the electrode interface. On the other hand, aptamer-Au-CuO-Cu_2O bioconjugate was prepared to amplify the cathodic photocurrent signal. In such a bioconjugate, Au nanoparticles provide the basis for aptamer immobilization by gold-sulfur interaction. Additionally, the photocurrent of CuO–Cu_2O modified electrode is obviously improved by the surface plasmon resonance effect of Au nanoparticles (Fig. S6). When the aptamer-Au-CuO-Cu_2O bioconjugate is introduced on the P4/BSA/Ab/EDC-NHS/CDs-GO/GCE surface, the photocurrent increases dramatically (curve g in Fig. 3C), leading to an amplified signal. However, the blank control experiment indicated that the photocurrent of BSA/Ab/EDC-NHS/CDs-GO/GCE in the absence of P4 is not obviously changed after introducing the bioconjugate (Fig. S7).

3.4. Optimization of biosensor

Before constructing the biosensor, we studied the influence of the content of GO in the CDs-GO composites on the PEC response of the CDs-GO modified electrode. As shown in Fig. S8, the photocurrent of CDs-GO/GCE increases continually with increasing the content of GO from 6% to 12%. When the content of GO exceeds 12%, the photocurrent response declines. This is due to the fact that excessive GO in the nanocomposites affects the visible absorption of photoactive CDs. Moreover, excessive GO can act as charge recombination center that reduces the lifetime of photogenerated electron-hole pairs. Thus, 12% GO was used for the preparation of CDs-GO modified electrode in this work unless otherwise indicated.

Further, the electrode modified with CDs-GO composites containing 12% GO was employed to construct the biosensor, which was represented by the sandwich structure of aptamer-Au-CuO-Cu_2O/P4/Ab/CDs-GO/GCE. In such a sandwich assay, Ab and aptamer played crucial roles, and thus their concentrations affecting the PEC responses of biosensor towards 100 nM P4 were studied. The maximum photocurrent is achieved on the sensor constructed with 8 μg mL^{-1} Ab (Fig. S9) and 0.1 μM aptamer (Fig. S10). Excessive Ab or aptamer exhibits steric hindrance effect which reduces the photocurrent. Meanwhile, the time for the incubation between aptamer-Au-CuO-Cu_2O bioconjugate and P4/Ab/CDs-GO electrode also had an obvious impact on the sensing

performance. The PEC response increases with the incubation time from 10 min and reaches the saturation until 40 min (Fig. S11). So, 40 min was chosen as the appropriate time for the PEC detection.

3.5. PEC aptasensing of P4

Under optimized experimental conditions (Table S1), the PEC response of the proposed biosensor toward different concentrations of P4 were recorded at a bias potential of 0 V. We selected 0 V as the applied potential, considering that: (1) the fabricated CDs-GO/GCE could generate obvious cathodic current at 0 V; and (2) 0 V was a low potential value that could avoid high background and the interference of some oxidation/reduction reactions arising from high bias potential employed in many PEC sensors (Gao et al., 2019). Fig. 4A shows that the cathodic photocurrent increases with increasing the P4 concentration, manifesting that more photosensitive Au–CuO–Cu_2O nanocomposites are incorporated on the electrode surface to achieve the signal amplification. Further observation shows that a linear relationship exists between the cathodic photocurrent and the P4 concentration ranging from 0.5 nM to 180 nM (Fig. 4B). The linear regression equation is expressed as PI/μA = –(0.0096 ± 0.0003)*C*/nM – (0.190 ± 0.005), with a correlation coefficient of $R^2 = 0.998$. The detection limit (3S/N) is calculated to be 0.17 nM. Compared with many previously reported sensors for P4 determination (Table S2), the fabricated sandwich-type PEC biosensor exhibits an acceptable linear range and a low detection limit.

The interference studies were carried out to evaluate the specificity of the proposed PEC sensor by recording the photocurrent towards 100 nM P4 in the existence of some other hormones such as E1, E2, E3, EP, EE2 and DES at the same concentration level. All these hormones do not show obvious interference in the determination of P4 (Fig. 4C), indicating excellent selectivity of the fabricated sandwich PEC sensor. This can be ascribed to the specific affinity of P4-bingding Ab and aptamer with target P4 molecules.

The reproducibility of the proposed biosensor was assessed by checking the cathodic PEC responses of five independently prepared aptamer-Au-CuO-Cu_2O/P4/Ab/CDs-GO/GCE incubated with 100 nM P4 (Fig. S12). The relative standard deviation (RSD) is obtained to be 2.6%, indicating a good reproducibility of the analysis platform. In addition, the photocurrent response of the modified electrodes stored in a refrigerator at 4 °C was measured every three days (Fig. S13). The results show that the PEC sensor still maintains at least 94.2% of its initial response after fifteen days of storage, suggesting satisfactory storage stability of the proposed PEC sensor.

The cathodic PEC biosensor was employed to determine P4 in human serum samples acquired from Hospital of Huazhong University of Science and Technology. Prior to analysis, the serum samples were diluted 20 times with PBS (pH 7.4) referring to previous reports (Cash et al., 2009; Wang et al., 2017), and then filtered through 0.22-μm nylon membrane filters. The standard P4 solution at a certain concentration was spiked into the diluted serum samples and the photocurrent responses of the fabricated electrodes were recorded. As listed in Table S3, the recoveries are in the range from 92.5% to 106.7% and the RSD values are less than 3.2%, demonstrating the feasibility of the designed method for P4 determination in real samples with acceptable accuracy.

4. Conclusions

In summary, we proposed a cathodic sandwich Ab-aptamer-based PEC biosensor for selective P4 detection by using CDs-GO composites as photoactive materials and aptamer-Au-CuO-Cu_2O bioconjugate as PEC amplifier. The CDs-GO composites showed considerable cathodic photocurrent response while the aptamer-Au-CuO-Cu_2O bioconjugate combined the advantages of photoactive CuO–Cu_2O heterojunction, plasmonic Au nanoparticles and high-affinity aptamer. With the incubation of P4 as connection center, enhanced cathodic photocurrent response was obtained. Accordingly, a visible light-driven sandwich-

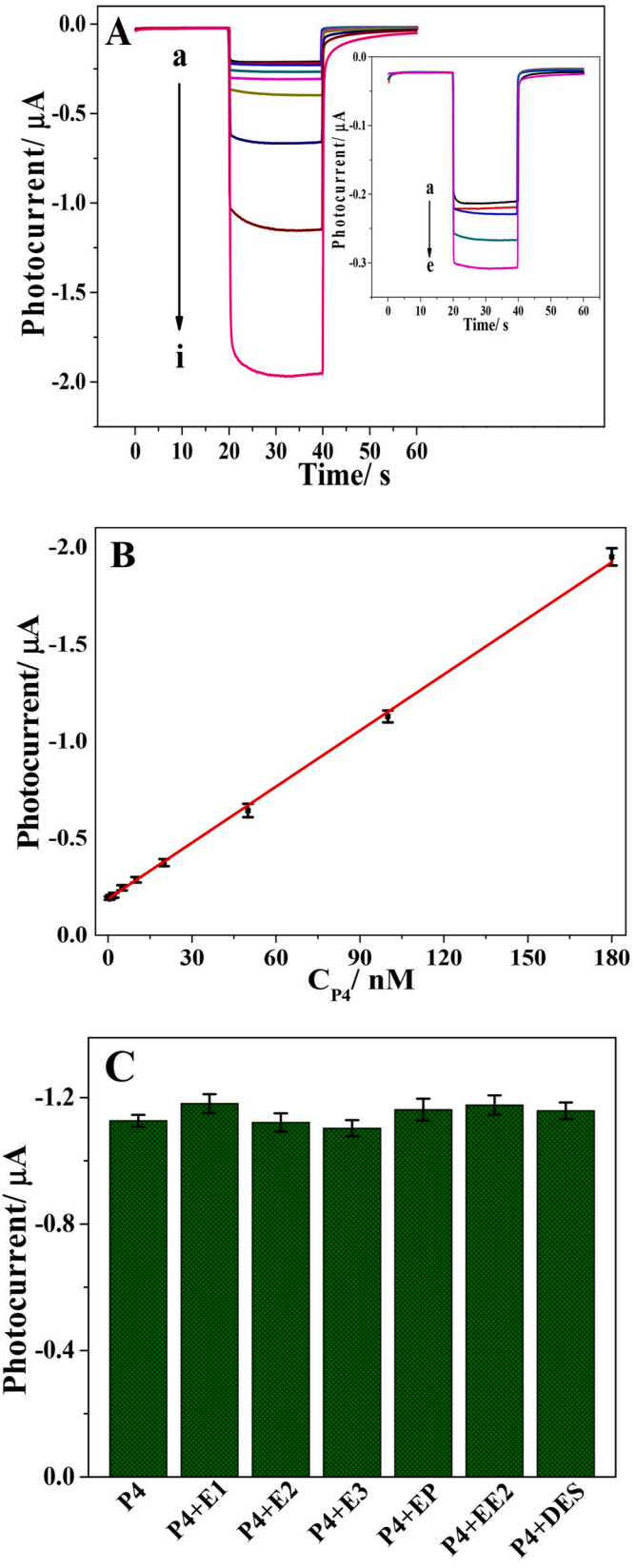

Fig. 4. (A) Photocurrent responses of the fabricated PEC sensor in 0.1 M PBS (pH 7.4) after incubation with different concentrations of P4: (a) 0.5, (b) 1, (c) 2, (d) 5, (e) 10, (f) 20, (g) 50, (h) 100 and (i) 180 nM. Inset: enlarged region of (a–e). (B) Calibration curve for P4 on the PEC sensor. (C) Histogram for photocurrent responses of PEC sensor incubation with 100 nM P4 containing equal amount of other hormones.

type PEC bioassay for highly sensitive and selective detection of P4 with acceptable reproducibility and stability was established through a photoactive nanomaterials-based signal amplification strategy. This work demonstrates that CDs with good photocathodic performance are useful for the construction of cathodic PEC biosensor. Moreover, the sandwich assay using aptamer-conjugated p-type semiconductors as signal-amplified element provides a new approach to the development of highly sensitive and selective cathodic PEC sensing platform.

Declaration of competing interest

The authors declare that they have no known competing financial interests or personal relationships that could have appeared to influence the work reported in this paper.

CRediT authorship contribution statement

Yuhan Zhu: Investigation, Data curation, Writing - original draft. **Zuwei Xu:** Methodology, Writing - review & editing. **Jie Gao:** Methodology, Writing - review & editing. **Weihao Ji:** Methodology, Writing - review & editing. **Jingdong Zhang:** Supervision, Funding acquisition, Writing - review & editing.

Acknowledgements

This work was supported by the National Natural Science Foundation of China (Grant No. 61571198) and the opening fund of Hubei Key Laboratory of Bioinorganic Chemistry & Materia Medica (Grant No. BCMM201902). We also thank the Analytical and Testing Center of Huazhong University of Science and Technology for help in materials characterization.

Appendix A. Supplementary data

Supplementary data to this article can be found online at https://doi.org/10.1016/j.bios.2020.112210.

References

Alhadrami, H.A., Chinnappan, R., Eissa, S., Rahamn, A.A., Zourob, M., 2017. Anal. Biochem. 525, 78–84.
Cash, K.J., Heeger, A.J., Plaxco, K.W., Xiao, Y., 2009. Anal. Chem. 81, 656–661.
Claus, R., Karg, H., Zwiauer, D., Von Butler, I., Pirchner, F., Rattenberger, E., 1983. Br. Vet. J. 139, 29–37.
Dai, D., Wolf, D.M., Litman, E.S., White, M.J., Leslie, K.K., 2002. Canc. Res. 62, 881–886.
Das, A., Sangaranarayanan, M.V., 2018. Sens. Actuators, B 256, 775–789.
Doldán, X., Fagúndez, P., Cayota, A., Laíz, J., Tosar, J.P., 2016. Anal. Chem. 88, 10466–10473.
Du, G., Zhang, D., Xia, B., Xu, L., Wu, S., Zhan, S., Ni, X., Zhou, X., Wang, L., 2016. Microchim. Acta 183, 2251–2258.
Erny, R., Pigne, A., Prouvost, C., Gamerre, M., Malet, C., Serment, H., Barrat, J., 1986. Am. J. Obstet. Gynecol. 154, 525–529.
Fan, D., Bao, C., Khan, M.S., Wang, C., Zhang, Y., Liu, Q., Zhang, X., Wei, Q., 2018. Biosens. Bioelectron. 106, 14–20.
Fan, D., Ren, X., Wang, H., Wu, D., Zhao, D., Chen, Y., Wei, Q., Du, B., 2017. Biosens. Bioelectron. 87, 593–599.
Fan, G.C., Shi, X.M., Zhang, J.R., Zhu, J.J., 2016. Anal. Chem. 88, 10352–10356.
Gao, J., Chen, Y., Ji, W., Gao, Z., Zhang, J., 2019. Analyst 144, 6617–6624.
Gevaerd, A., Blaskievicz, S.F., Zarbin, A.J., Orth, E.S., Bergamini, M.F., Marcolino-Junior, L.H., 2018. Biosens. Bioelectron. 112, 108–113.
Golub, E., Albada, H.B., Liao, W.C., Biniuri, Y., Willner, I., 2015. J. Am. Chem. Soc. 138, 164–172.
Golub, E., Pelossof, G., Freeman, R., Zhang, H., Willner, I., 2009. Anal. Chem. 81, 9291–9298.
Grabar, K.C., Freeman, R.G., Hommer, M.B., Natan, M.J., 1995. Anal. Chem. 67, 735–743.
Graham, J.D., Clarke, C.L., 1997. Endocr. Rev. 18, 502–519.
Greendale, G.A., Reboussin, B.A., Hogan, P., Barnabei, V.M., Shumaker, S., Johnson, S., Barrett-Connor, E., 1998. Obstet. Gynecol. 92, 982–988.
Hargrove, J.T., Maxson, W.S., Wentz, A.C., Burnett, L.S., 1989. Obstet. Gynecol. 73, 606–612.
Herzog, A.G., 1995. Neurology 45, 1660–1662.
Hontoria-Lucas, C., López-Peinado, A.J., López-González, J.D., Rojas-Cervantes, M.L., Martin-Aranda, R.M., 1995. Carbon 33, 1585–1592.
Hu, C., Li, M., Qiu, J., Sun, Y.P., 2019. Chem. Soc. Rev. 48, 2315–2337.
Iliuk, A.B., Hu, L., Tao, W.A., 2011. Anal. Chem. 83, 4440–4452.
Jain, P.K., El-Sayed, I.H., El-Sayed, M.A., 2007. Nano Today 2, 18–29.
Jana, N.R., Gearheart, L., Murphy, C.J., 2001. Adv. Mater. 13, 1389–1393.
Kim, J.J., Kurita, T., Bulun, S.E., 2013. Endocr. Rev. 34, 130–162.
Li, H., Su, Z., Hu, S., Yan, Y., 2017. Appl. Catal., B 207, 134–142.
Li, Z., Chen, F., Yuan, L., Liu, Y., Zhao, Y., Chai, Z., Shi, W., 2012. Chem. Eng. J. 210, 539–546.
Li, Z., Zhang, J., Li, Y., Zhao, S., Zhang, P., Zhang, Y., Bi, J., Liu, G., Yue, Z., 2018. Biosens. Bioelectron. 99, 251–258.
Lishko, P.V., Botchkina, I.L., Kirichok, Y., 2011. Nature 471, 387.
Liu, S., Cao, H., Wang, Z., Tu, W., Dai, Z., 2015. Chem. Commun. 51, 14259–14262.
Liu, Y., Zhou, L., Li, Y., Deng, R., Zhang, H., 2017. Nanoscale 9, 491–496.
Mazumder, V., Chi, M., More, K.L., Sun, S., 2010. Angew. Chem. Int. Ed. 49, 9368–9372.
Murdoch, M., Waterhouse, G.I.N., Nadeem, M.A., Metson, J.B., Keane, M.A., Howe, R.F., Llorca, J., Idriss, H., 2011. Nat. Chem. 3, 489.
Ojoghoro, J.O., Chaudhary, A.J., Campo, P., Sumpter, J.P., Scrimshaw, M.D., 2017. Sci. Total Environ. 579, 1876–1884.
Qiu, Z., Shu, J., Tang, D., 2018. Anal. Chem. 90, 12214–12220.
Serafín, V., Martínez-García, G., Aznar-Poveda, J., Lopez-Pastor, J.A., Garcia-Sanchez, A. J., Garcia-Haro, J., Campuzano, S., Yáñez-Sedeño, P., Pingarrón, J.M., 2019. Anal. Chim. Acta 1049, 65–73.
Sharma, A.K., Kent, A.D., Heemstra, J.M., 2012. Anal. Chem. 84, 6104–6109.
Song, K., Ding, C., Zhang, B., Chang, H., Zhao, Z., Wei, W., Wang, J., 2018. Microchim. Acta 185, 310.
Song, S., Wang, L., Li, J., Fan, C., Zhao, J., 2008. Trac. Trends Anal. Chem. 27, 108–117.
Teng, F., Hu, K., Ouyang, W., Fang, X., 2018. Adv. Mater. 30, 1706262.
Tölgyesi, Á., Verebey, Z., Sharma, V.K., Kovacsics, L., Fekete, J., 2010. Chemosphere 78, 972–979.
Trapiella-Alfonso, L., Costa-Fernández, J.M., Pereiro, R., Sanz-Medel, A., 2011. Biosens. Bioelectron. 26, 4753–4759.
Travlou, N.A., Giannakoudakis, D.A., Algarra, M., Labella, A.M., Rodríguez-Castellón, E., Bandosz, T.J., 2018. Carbon 135, 104–111.
Wang, J., Long, J., Liu, Z., Wu, W., Hu, C., 2017. Biosens. Bioelectron. 91, 53–59.
Wei, L., Borowiec, J., Zhu, L., Zhang, J., 2011. Microchim. Acta 173, 439–443.
Willner, I., Zayats, M., 2007. Angew. Chem. Int. Ed. 46, 6408–6418.
Wu, L., Xiong, E., Zhang, X., Zhang, X., Chen, J., 2014a. Nano Today 9, 197–211.
Wu, W., Li, J., Pan, D., Li, J., Song, S., Rong, M., Li, Z., Gao, J., Lu, J., 2014b. ACS Appl. Mater. Interfaces 6, 16974–16981.
Xu, M., He, G., Li, Z., He, F., Gao, F., Su, Y., Zhang, L., Yang, Z., Zhang, Y., 2014. Nanoscale 6, 10307–10315.
Yuan, F., Li, S., Fan, Z., Meng, X., Fan, L., Yang, S., 2016. Nano Today 11, 565–586.
Zhang, J., Sun, Y., Xu, B., Zhang, H., Gao, Y., Zhang, H., Song, D., 2013. Biosens. Bioelectron. 45, 230–236.
Zhang, J., Yu, S.H., 2016. Mater. Today 19, 382–393.
Zhang, K., Fent, K., 2018. Sci. Total Environ. 610, 1164–1172.
Zhang, M., Bai, L., Shang, W., Xie, W., Ma, H., Fu, Y., Fang, D., Sun, H., Fang, L., Han, M., Liu, C., Yang, S., 2012. J. Mater. Chem. 22, 7461–7467.
Zhao, T., Liu, R., Ding, X., Zhao, J., Yu, H., Wang, L., Xu, Q., Wang, X., Lou, X., He, M., Xiao, Y., 2015. Anal. Chem. 87, 7712–7719.
Zhao, W.W., Xu, J.J., Chen, H.Y., 2018. Anal. Chem. 90, 615–627.
Zhu, S., Meng, Q., Wang, L., Zhang, J., Song, Y., Jin, H., Zhang, K., Sun, H., Wang, H., Yang, B., 2013. Angew. Chem. Int. Ed. 52, 3953–3957.
Zhu, Y., Xu, Z., Yan, K., Zhao, H., Zhang, J., 2017. ACS Appl. Mater. Interfaces 9, 40452–40460.
Zuo, X., Xiao, Y., Plaxco, K.W., 2009. J. Am. Chem. Soc. 131, 6944–6945.